Pergamon

Int. J. Heat Mass Transfer. Vol. 41, No. 1, pp. 61–72, 1998

Printed in Great Britain
0017–9310/98 $19.00+0.00

PII: S0017-9310(97)00111-7

Developing mixed convection in a coiled heat exchanger

J. J. M. SILLEKENS, C. C. M. RINDT† and A. A. VAN STEENHOVEN

Eindhoven University of Technology, Faculty of Mechanical Engineering, P.O. Box 513, 5600 MB Eindhoven, The Netherlands

(*Received* 13 *September* 1996 *and in final form* 7 *April* 1997)

Abstract—In this paper the development of mixed convection in a helically coiled heat exchanger for $Re = 500$, $Pr = 5$ and $\delta = 1/14$ is studied. The influence of buoyancy forces ($Gr = \mathcal{O}(10^5)$) on heat transfer and secondary flow is analyzed. In the method used the parabolized equations are solved using a finite difference discretization. The code is tested on mixed convection flow in a 90° curved tube of which the results are compared to the results obtained with an elliptical code. For the helically coiled tube a constant wall temperature is considered. It appeared that heat transfer is highly influenced by secondary flow induced by centrifugal and buoyancy forces. For low Grashof numbers a splitting phenomenon of the temperature field is observed due to large secondary velocities, resulting in two separated areas of fluid. For high Grashof numbers the fluid in the coiled pipe becomes almost linearly startified which results in small secondary velocities. A wavy behaviour in the Nusselt number is observed for medium Grashof numbers.

INTRODUCTION

Helically coiled tubes are widely used in heat exchange systems, since they are relatively easy to produce, cheap and efficient. A typical example can be found in the storage vessel of a solar domestic hot water system (SDHWS), but many other technical applications of helical heat exchangers can be found. When a SDHWS is operated according to the low-flow principle [1], a laminar flow occurs and both buoyancy and centrifugal forces give rise to a secondary flow perpendicular to the main axial flow. The efficiency of helically coiled heat exchangers is largely influenced by this secondary flow through which temperature boundary layers remain thin and the rate of heat transfer increases.

In a horizontally curved pipe centrifugal forces lead to a secondary flow with a horizontal orientation resulting in the so-called Dean vortices [2]. Buoyancy forces in a heated pipe, however, lead to a secondary flow with a vertical orientation, resulting in the so-called Morton vortices [3]. Intuitively one might expect that the resulting secondary flow in a heated horizontally curved pipe is tilted with respect to the horizontal. Considering the driving mechanism it is possible to make a first estimate of the magnitude of the secondary flow in a curved pipe. For the secondary flow due to centrifugal forces, one may set up a balance between the work done by centrifugal forces and the resulting kinetic energy of the secondary flow (neglecting dissipation) leading to:

$$\frac{\bar{u}_{Dn}}{\bar{u}_{ax}} = \mathcal{O}\left(\frac{Dn}{Re}\right) \tag{1}$$

with the Reynolds number defined as $Re = \bar{u}_{ax} \cdot d/\nu$ and the Dean number as $Dn = Re \cdot \delta^{1/2}$ (δ being the curvature ratio of the tube). Analogous for the secondary flow due to buoyancy forces, a balance may be set up between work done by specific buoyancy forces and the resulting specific kinetic energy of the secondary flow which gives:

$$\frac{\bar{u}_{Gr}}{\bar{u}_{ax}} = \mathcal{O}\left(\frac{\sqrt{Gr}}{Re}\right) \tag{2}$$

with $Gr = (g \cdot \beta/\nu^2) \cdot \Delta T \cdot d^3$ being the Grashof number. It is expected, that the secondary flow due to buoyancy forces for high Prandtl number fluids is lower than for low Prandtl number fluids. High Prandtl number fluids give rise to smaller temperature boundary layers and thus the effect of viscosity will be more pronounced, reducing the velocity. From a similarity formulation for the boundary layer equations governing buoyancy induced flow at a vertical plate [4], it was found that the upward flow is proportional to $1/\sqrt{1+Pr}$ ($Pr = \nu/\alpha$). Taking into account this Prandtl number effect we find:

$$\frac{\bar{u}_{Gr}}{\bar{u}_{ax}} = \mathcal{O}\left(\frac{\sqrt{Gr}}{Re\sqrt{(1+Pr)}}\right). \tag{3}$$

Torsion effects induced by the pitch of a coil may cause a swirling secondary flow to develop [5]. The magnitude of this swirling flow can be estimated by:

†Author to whom correspondence should be addressed.

NOMENCLATURE

d	diameter of tube	$\bar{u}_{ax}$	mean axial velocity
Dn	Dean number	$\bar{u}_{Dn}$	'centrifugal' secondary velocity
g	acceleration due to gravity	$\bar{u}_{Gn}$	'pitch' secondary velocity
Gn	Germano number	$\bar{u}_{Gr}$	'buoyant' secondary velocity
Gr	Grashof number	x	axial coordinate.
$\bar{h}$	heat transfer coefficient		
K	'swirl' number		
Nu	Nusselt number	Greek symbols	
p	'cross-stream' pressure	α	thermal diffusivity
$\bar{p}$	'space-averaged' pressure	β	cubic expansion coefficient
p_c	pitch of coil	δ	curvature ratio of coil
Pr	Prandtl number	λ	heat conduction coefficient
r	radial coordinate	ν	kinematic viscosity
Ra	Rayleigh number	Ω	streamwise vorticity
Re	Reynolds number	ϕ	velocity potential
R_c	curvature radius of coil	ψ	streamfunction
T	temperature	θ	tangential coordinate.

$$\frac{\bar{u}_{Gn}}{\bar{u}_{ax}} = \mathcal{O}\left(\frac{Gn}{Re}\right) \tag{4}$$

with the Germano number defined as $Gn = Re \cdot \frac{1}{2} d \cdot p_c/(R_c^2 + p_c^2)$ (p_c being the pitch of the coil and R_c the curvature radius). For low Germano numbers (like in a SDHWS: $Gn \approx 3.6$) the influence of the pitch on the flow field may be neglected [6]. The physical situation in the heat exchanger of a SDHWS further is characterized by the following parameters: $Re \approx 500$, $\delta = 1/14$, $Gr = \mathcal{O}(10^5)$, $Pr \approx 5$. Using these values it is estimated that $\bar{u}_{Dn} < \bar{u}_{Gr} < \bar{u}_{ax}$, and thus centrifugal forces, buoyancy forces and pressure effects all have their influence on the flow field in the heat the exchanger.

Notwithstanding its practical importance, there appears to be a serious lack of knowledge concerning the development of mixed convection in curved pipes. Most studies are limited to fully developed heat and fluid flow (occurring for constant heat input) [7–9] or to the proximate part (less than 1 turn; see for example [10, 11]) of a curved pipe. In practical situations, however, flow is mostly not fully developed (in case of constant wall temperatures) and the major part of heat transfer occurs more downstream in the coiled heat exchanger. Therefore, a good understanding of developing heat and fluid flow is of great practical importance. The present study focuses on the development of laminar mixed convection flow in a helically coiled tube. Temperature and velocity fields are presented for axial distances towards the inlet up to 100 diameters (approximately two turns), and flow and heat transfer parameters up to 200 diameters. Also the influence of the driving force for natural convection, quantified by the Grashof number, is investigated.

NUMERICAL METHOD

When it is known that a flow has a dominant direction, the Navier–Stokes and energy equations (which are elliptic in space) can be parabolized in this so-called streamwise direction. The major advantage of parabolizing the equations is the opportunity to use a marching procedure: each cross-section is treated separately, using information of the previous one. This may considerably decrease the required computer capacities, especially when the computational domain in streamwise direction is relatively long.

Parabolized Navier–Stokes equations

The parabolized Navier–Stokes and energy equations are derived from the full equations by omission of shear stresses and diffusive fluxes acting in streamwise direction. This prohibits information from downstream to penetrate upstream and excludes the need for a downstream boundary condition. A further feature of the parabolized Navier–Stokes equations is the role that is played by the pressure. In order to exclude the elliptic interaction between pressure terms in the momentum equation with the terms in the continuity equation, the pressure derivatives are split up in a streamwise component $\partial\bar{p}/\partial x$ and in the cross-stream components $\partial p/\partial r$ and $1/r \cdot \partial p/\partial\theta$, which are treated quite differently [12]. The cross-stream pressure derivatives are linked to local continuity, whereas the streamwise pressure derivative is coupled to the streamwise velocity by requiring global continuity over each cross-stream plane. In this sense, the pressure $\bar{p}$ can be interpreted as a space averaged pressure over a cross-section, which is more or less the driving force behind the flow.

Assuming that the x-direction coincides with the

streamwise direction, the parabolized Navier–Stokes and energy equations, based on the Oberbeck–Boussinesq approximations, written in cylindrical polar coordinates, read (see Fig. 1):

continuity

$$\frac{u_r}{r}+\frac{\partial u_r}{\partial r}+\frac{\partial u_\theta}{r\,\partial\theta}+\frac{\partial u_x}{\partial x}=0 \tag{5}$$

r-momentum

$$u_r\frac{\partial u_r}{\partial r}+u_\theta\frac{\partial u_r}{r\,\partial\theta}-\frac{u_\theta^2}{r}+u_x\frac{\partial u_r}{\partial x}=-\frac{\partial p}{\partial r}$$
$$+Re^{-1}\left[\frac{\partial u_r}{r\,\partial r}-\frac{u_r}{r^2}+\frac{\partial^2 u_r}{\partial r^2}+\frac{\partial^2 u_r}{r^2\,\partial\theta^2}-\frac{2\,\partial u_\theta}{r^2\,\partial\theta}\right]$$
$$-\frac{u_x^2}{R_c-r\sin\theta}\sin\theta+\frac{Gr}{Re^2}T\cos\theta \tag{6}$$

θ-momentum

$$u_r\frac{\partial u_\theta}{\partial r}+u_\theta\frac{\partial u_\theta}{r\,\partial\theta}+\frac{u_r u_\theta}{r}+u_x\frac{\partial u_\theta}{\partial x}=-\frac{\partial p}{r\,\partial\theta}$$
$$+Re^{-1}\left[\frac{\partial u_\theta}{r\,\partial r}-\frac{u_\theta}{r^2}+\frac{\partial^2 u_\theta}{\partial r^2}+\frac{\partial^2 u_\theta}{r^2\,\partial\theta^2}+\frac{2\,\partial u_r}{r^2\,\partial\theta}\right]$$
$$-\frac{u_x^2}{R_c-r\sin\theta}\cos\theta-\frac{Gr}{Re^2}T\sin\theta \tag{7}$$

x-momentum

$$u_r\frac{\partial u_x}{\partial r}+u_\theta\frac{\partial u_x}{r\,\partial\theta}+u_x\frac{\partial u_x}{\partial x}=-\frac{\partial\bar{p}}{\partial x}$$
$$+Re^{-1}\left[\frac{\partial u_x}{r\,\partial r}+\frac{\partial^2 u_x}{\partial r^2}+\frac{\partial^2 u_x}{r^2\,\partial\theta^2}\right] \tag{8}$$

energy

$$u_r\frac{\partial T}{\partial r}+u_\theta\frac{\partial T}{r\,\partial\theta}+u_x\frac{\partial T}{\partial x}$$
$$=(RePr)^{-1}\left[\frac{\partial T}{r\,\partial r}+\frac{\partial^2 T}{\partial r^2}+\frac{\partial^2 T}{r^2\,\partial\theta^2}\right]. \tag{9}$$

Like in ref. [13], terms of order $\mathcal{O}(\delta)$ smaller than the leading terms are omitted in the equations.

In order to eliminate the cross-stream pressure derivatives the r and θ momentum equations are cross-differentiated: $1/r\cdot\partial/\partial\theta\times(r\text{-momentum})-(1/r\cdot\partial/\partial r\cdot r\times(\theta\text{-momentum})$ yielding an equation for the streamwise component of the vorticity Ω:

$$u_r\frac{\partial\Omega}{\partial r}+u_\theta\frac{\partial\Omega}{r\,\partial\theta}+u_x\frac{\partial\Omega}{\partial x}-\frac{\partial u_x}{\partial x}\Omega$$
$$+\frac{\partial u_x}{r\,\partial\theta}\frac{\partial u_r}{\partial x}-\frac{\partial u_x}{\partial r}\frac{\partial u_\theta}{\partial x}$$
$$=Re^{-1}\left[\frac{\partial\Omega}{r\,\partial r}+\frac{\partial^2\Omega}{\partial r^2}+\frac{\partial^2\Omega}{r^2\,\partial\theta^2}\right]$$
$$+\frac{2u_x}{R_c-r\sin\theta}\left[\frac{\partial u_x}{\partial r}\cos\theta-\frac{\partial u_x}{r\,\partial\theta}\sin\theta\right]$$
$$+\frac{Gr}{Re^2}\left[\frac{\partial T}{\partial r}\sin\theta+\frac{\partial T}{r\,\partial\theta}\cos\theta\right] \tag{10}$$

where Ω is defined as $\Omega=1/r\cdot\partial u_r/\partial\theta-1/r\cdot\partial(ru_\theta)/\partial r$. From equation (10) it is seen that centrifugal forces and buoyancy forces (the last two terms in the equation), as it were, play a role as vorticity generators.

When further a velocity potential ϕ and a stream-function ψ are defined by:

$$u_r=\frac{\partial\phi}{\partial r}+\frac{\partial\psi}{r\,\partial\theta}\quad\text{and}\quad u_\theta=\frac{\partial\phi}{r\,\partial\theta}-\frac{\partial\psi}{\partial r} \tag{11}$$

then the continuity equation is replaced by

$$\frac{\partial^2\phi}{\partial r^2}+\frac{\partial\phi}{r\,\partial r}+\frac{\partial^2\phi}{r^2\,\partial\theta^2}=-\frac{\partial u_x}{\partial x} \tag{12}$$

in combination with the following equation for Ω:

$$\frac{\partial^2\psi}{\partial r^2}+\frac{\partial\psi}{r\,\partial r}+\frac{\partial^2\psi}{r^2\,\partial\theta^2}=\Omega. \tag{13}$$

Equations (5)–(9) are thus replaced by equations (12), (13), (10), (8) and (9).

Numerical solution procedure

The numerical method used for solving the equations presented above, is a modification of the code presented in ref. [14]. It is based on a standard second-order finite difference method [15]. The obtained set of algebraic equations is solved by an alternating direction implicit method [12]. Although the governing equations are physically coupled, in the solution procedure each equation is treated independently, and the coupling finds place via an iterative loop over the equations as sketched in Fig. 2.

At the first cross-section initial (boundary) values are prescribed for the velocity and the temperature. These values are used as a first guess for the solution at the following cross-section and for the evaluation of the axial derivatives in the equations. Then equation (8) is solved and the axial pressure gradient is adjusted by means of a secant method [16] such that global continuity is preserved. The next step is to

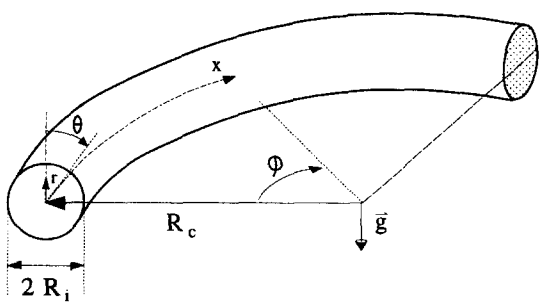

Fig. 1. Horizontally curved pipe: definitions and geometry.

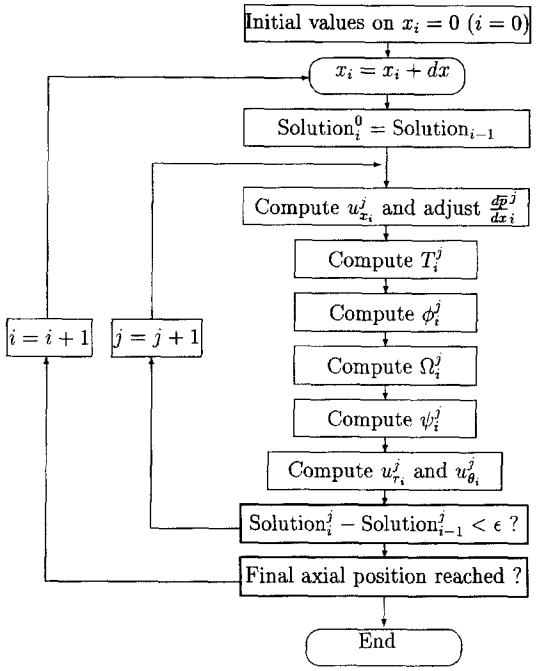

Fig. 2. Iterative solution procedure.

compute the temperature field [equation (9)]. Then the velocity potential [equation (12)] followed by the vorticity [equation (10)] and the streamfunction [equation (13)] are computed. Finally, equations (11) are employed to calculate the secondary flow components. The solution procedure is repeated until convergence has been reached.

At each cross-section, boundary conditions are needed for the velocity and the temperature. The velocity is supposed to be zero at the wall according to the no-slip condition. Therefore, the following boundary conditions for the axial velocity, the streamfunction, the potential and the axial vorticity are prescribed at the pipe wall:

$$u_x|_R = 0 \quad \psi|_R = 0 \quad \left.\frac{\partial \phi}{\partial r}\right|_R = 0 \quad \Omega|_R = \frac{\partial^2 \psi}{\partial r^2} + \frac{1}{R^2}\frac{\partial \phi}{\partial \theta} \tag{14}$$

with $R = 1/2d$. In the boundary condition for $\Omega|_R$ use is made of

$$\left.\frac{\partial \psi}{\partial r}\right|_R = \frac{1}{R}\left.\frac{\partial \phi}{\partial \theta}\right|_R$$

implying that $u_\theta|_R = 0$.

When discretizing $\Omega|_R$ the term $\partial^2\psi/\partial r^2$ is approximated by:

$$\left.\frac{\partial^2 \psi}{\partial r^2}\right|_R = \frac{\psi_{R-\Delta r} - \psi_R}{\frac{1}{2}(\Delta r)^2} + \frac{\Delta r \left.\frac{\partial \psi}{\partial r}\right|_R}{\frac{1}{2}(\Delta r)^2} \tag{15}$$

with Δr the grid distance in radial direction. In the latter equation again

$$\left.\frac{\partial \psi}{\partial r}\right|_R = \frac{1}{R}\left.\frac{\partial \phi}{\partial \theta}\right|_R$$

is substituted. The temperature is set to a value dependent on the problem solved (constant or linearly varying with axial position).

The parabolic equations are discretized using 40×180 points in $r \times \theta$ direction. For the 90° curved tube, of which the results are compared to the ones obtained with an elliptical code, 500 marching steps were employed. Mesh refinement to 80×360 points using 1000 marching steps showed a relative variation in the computed Nusselt number of less than 1%. For the coiled heat exchanger 7500 marching steps were employed to resolve an axial domain of $200d$ (about four turns). The axial discretization was refined five times near the entrance of the coil. The computations were performed on a Silicon Graphics Super Challenge (MIPS R4400 processor). For the 90° curved tube each computation took approximately 2.5 h CPU-time.

Comparison between elliptic and parabolic results

For validation of the parabolic code, results were obtained for mixed convection in a 90° curved tube and compared to elliptically computed ones. For details about the elliptical code used, one is referred to refs. [17, 18]. The domain consisted of a $2d$ straight inflow section and a $11d$ (90°) curved section with curvature ratio $\delta = 1/14$. At the entrance ($x = -2d$) the Hagen–Poiseuille velocity profile for fully developed pipe flow is assumed. The dimensionless temperature of the inflowing medium is set to $T_{\text{inlet}} = 1$. The medium is cooled by the tube wall to $T_{\text{wall}} = 0$. At the wall a gradual decrease following a cosine function $(1/2\,\lambda)$ of the temperature $T = 1$ at $x = -1/2d$ to $T = 0$ at $x = 1/2d$ is given to prevent a singularity at $x = 0$. The calculations were carried out for a Prandtl number $Pr = 5$ (water), a Reynolds number $Re = 500$ and a Grashof number $Gr = 10^5$.

In Fig. 3 the parabolically computed velocity and temperature fields are shown. The velocity field is visualized by isotachs for the axial component and by velocity vectors for the secondary components. The difference in velocity magnitude between the different isotachs equals $0.2 \cdot \bar{u}_{ax}$. The scaling of the secondary flow is such that a vector length equal to the diameter of the pipe corresponds to twice the average axial velocity. The temperature field is visualized by contours of equal temperature. The difference between the successive isotherms is 0.1, where the temperature at the wall is equal to 0.

At $x = d$ the flow is forced towards the outer bend due to centrifugal forces, resulting in a Dean type secondary flow. More downstream it is seen how the velocity field is affected by buoyancy forces. The medium is cooled at the tube wall and thus experiences a force

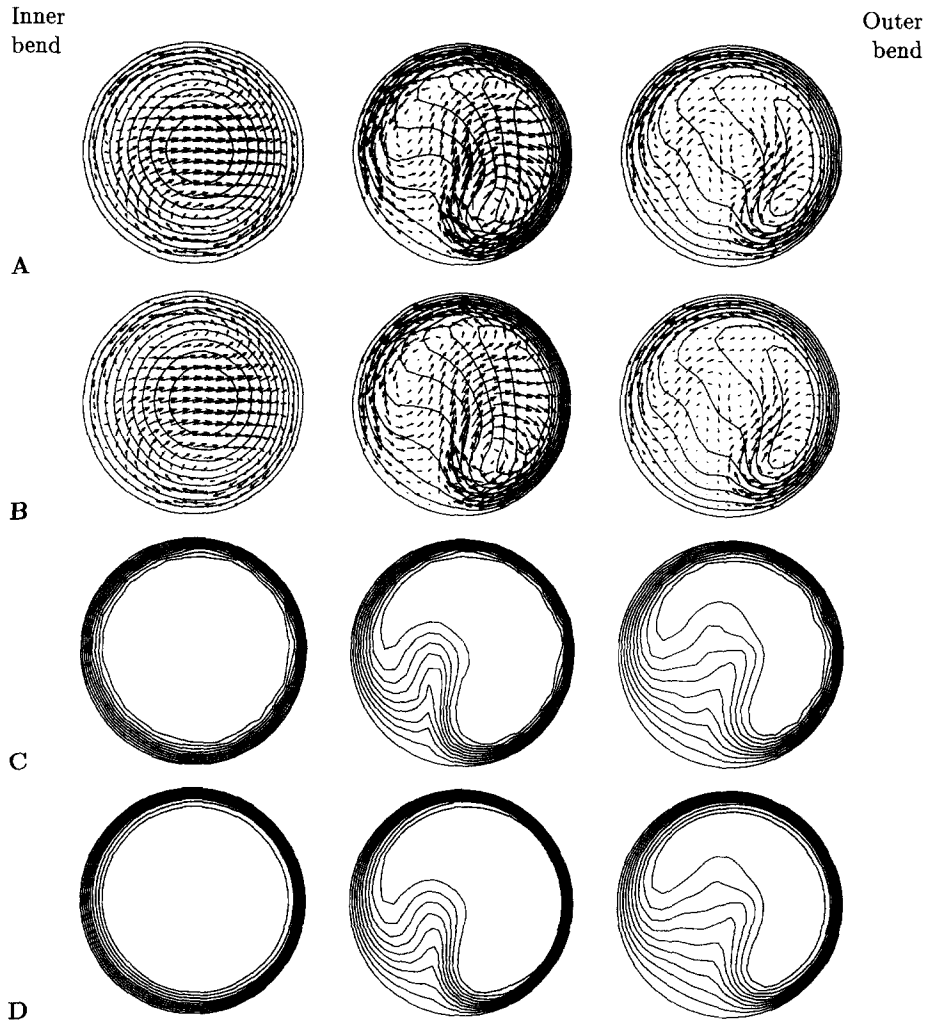

Fig. 3. Velocity and temperature fields at cross-section $x = d$ (left), $x = 4d$ and at $x = 8d$ (right) for $Re = 500$, $Dn = 134$, $Pr = 5$, $Gr = 10^5$. (A) elliptically computed velocity field; (B) parabolically computed velocity field; (C) elliptically computed temperature field; (D) parabolically computed temperature field.

downwards near the wall. This may result in symmetric Morton vortices in a straight tube. However, due to the interaction of buoyancy and centrifugal forces, the flow loses all symmetry. From the direction of the secondary flow it can be derived that the centrifugal effects are dominant over the buoyancy effects near the entrance of the curved pipe (at $x = d$), whereas more downstream the buoyancy forces seem to be more important. This is due to the fact that centrifugal forces are present from the beginning of the bend, whereas a temperature boundary layer first has to grow to give rise to buoyancy forces. Besides, in Fig. 3 the influence of the secondary flow field on the temperature field is clearly visible, resulting in relatively thin thermal boundary layers near the right-upper wall and relatively thick ones near the left-bottom wall. For a more detailed description of the flow and temperature fields one is referred to refs. [17, 18].

A great similarity between the elliptically computed results and the parabolic results is noticed. In the velocity field at $x = 8d$ even a subtle phenomenon as the third vortex is present. In the temperature field some differences can be observed, but these are most likely due to interpolation errors produced in the post-processing of the results rather than to differences in the solution. The stream of cooled water flowing into the core of the pipe is shown to be approximately equal, and thus the differences in heat transfer between the elliptic and parabolic results are expected to be small. The relative differences between the elliptic and parabolic results in terms of the Nusselt number and K-number (a measure for the strength of the secondary flow field; see the section on flow and heat transfer parameters, for its definition) amount to maximal 6 and 10%, respectively, where the Nusselt and K-number reach their local maxima. The relative difference in bulk temperature remains less than 1%. In refs. [17, 18] a detailed description is given of the development of the flow and heat transfer parameters as function of axial position.

The parabolic procedure is also tested on the problem of forced convection in a horizontal straight tube (known as the Graetz problem). The domain extended from $x = -d$ towards $x = 200d$. The discretization and the boundary conditions were the same as described for the 90° curved tube except for the inflow condition which was a plug flow instead of a Hagen–Poiseuille flow. The calculations were performed at a Reynolds number of $Re = 500$ and a Prandtl number of $Pr = 5$. The relative difference in the computed Nusselt number or bulk temperature with the solution given by ref. [19] is maximal 3%, at $x = 200d$, which again is an indication that the method is quite accurate. Also the simultaneous development of the velocity and temperature field from plug flow to Hagen–Poiseuille flow was accurately described by the parabolic procedure. The maximum relative difference in the local Nusselt number with the elliptic results of ref. [20] was 4%, and the maximum relative difference in the local Fanning friction factor with the elliptic results of Schmidt (given by ref. [19]) for this situation was 3%.

Preliminary stability analysis of the flow

In order to check whether or not the physical situation investigated could indeed be described by the stationary equations, for the 90° curved tube the time dependent Navier–Stokes and energy equations were solved at $Gr = 10^5$ using a Cranck–Nicholson scheme for the discretization of the time derivatives. The steady solution was perturbed at the first time step by increasing the Grashof number momentarily to $Gr = 10^6$. The time step was chosen such that the Brunt–Väisälä time scale was resolved by 30 time steps. The time dimensionless Brunt–Väisälä time scale is given by $\theta_{BV} = (Re/Gr) \cdot (\bar{u}_{ax}/d)$, and the corresponding Brunt–Väisälä frequency f_{BV} is equal to $1/\theta_{BV}$. The Brunt–Väisälä frequency is an indication (in fact it is an over estimation [21]) of the characteristic frequency of gravity waves, which might occur in the flow. It can be expected that if buoyancy forces give rise to time dependency of the flow, the Brunt–Väisälä frequency will be the mode to be resolved (see also ref. [22], who experimentally found a first bifurcation to an unsteady air flow in a differentially heated cavity at $Gr \approx 5 \cdot 10^7$ with a frequency of $0.15 \cdot f_{BV}$). The first results, however, show that a development in time towards a steady solution takes place within $2 \cdot \theta_{BV}$, and hence with some caution it may, thus, be concluded that the flow is indeed steady.

RESULTS

In this section the development of isothermally cooled water flow in a coiled pipe will be analysed. The characteristic dimensionless variables are $Re = 500$, $Dn = 134$ ($\delta = 1/14$), $Pr = 5$ and $Gr = 0 - 10^6$, values related to the flow in a SDHWS.

Description of velocity and temperature fields

In Fig. 4 the velocity field is shown at three axial positions: $x = 20d$ (at the left side of the page), $x = 50d$ and $x = 100d$ (at the right side of the page) and for four different values of the Grashof number: $Gr = 0$, $Gr = 10^5$, $Gr = 5 \cdot 10^5$ and $Gr = 10^6$. The velocity field is visualized by isotachs for the axial component and by velocity vectors for the secondary components and the scaling is the same as the one used in Fig. 3.

Figure 4A indicates that the velocity field for forced flow ($Gr = 0$) in a coiled pipe is almost fully developed at $x = 20d$, since there are only minor changes compared to $x = 50d$ or to $x = 100d$. The velocity field is characterized by two longitudinal Dean-type vortices and the axial velocity contours show the familiar C-shape.

The results obtained at higher Grashof numbers show how buoyancy effects take over from centrifugal effects at $x = 20d$, and decrease with increasing axial position, since buoyancy forces diminish due to the cooling of the fluid. In general the flow consists of two longitudinal vortices, but the orientation of these vortices differs substantially from case to case. At $x = 20d$ the axial velocity field possesses a maximum at the upper side of the pipe for $Gr = 5 \cdot 10^5$ and for $Gr = 10^6$. The influence of centrifugal effects are minimized due to the location of the maximal axial velocity since Dean-type flow is bounded by the tube wall. Furthermore, the major part of the medium in the tube is now stably stratified (as seen in Fig. 5C, D) and the centrifugal forces seem not strong enough to overcome this stabilizing effect. In fact there only is a thin fluid layer at the upper half of the tube where an unstable stratification exists. Since wall effects here are strong, and downward flow in the lower half of the tube is prevented by the stable stratification, only a relatively small downward Morton-type flow has grown. The velocity field for $Gr = 10^6$ at $x = 20d$ is remarkably similar to the two-vortex result obtained by ref. [23] for mixed convection in a straight tube at $Gr_\tau = 8 \cdot 10^5$. This indicates that initially the secondary flow for $Gr = 10^6$ is mainly governed by buoyancy forces. Also for $Gr = 5 \cdot 10^5$ and for $Gr = 10^6$, eventually buoyancy forces decrease and centrifugal forces begin to show their influence. This is observed at $x = 50d$ and $x = 100d$. At $x = 200d$ (not shown here), the velocity field is almost equal to the velocity field for $Gr = 0$ at $x = 100d$ (fully developed Dean-type flow).

In Fig. 5 the development of the temperature field is visualized by contours of equal temperature at axial positions $x = 20d$, $x = 50d$ and $x = 100d$. The difference between the successive isotherms is 0.1, where the temperature at the wall is equal to 0. For $Gr = 5 \cdot 10^5$ and for $Gr = 10^6$ the water in the tube at $x = 100d$ was cooled that much that even the isotherm of 0.1 was not visible. In these cases, the difference between successive isotherms was set at 0.02.

Considering, first, the flow in the coil without buoyancy effects (Fig. 5A), it is seen that at $x = 20d$ the C-

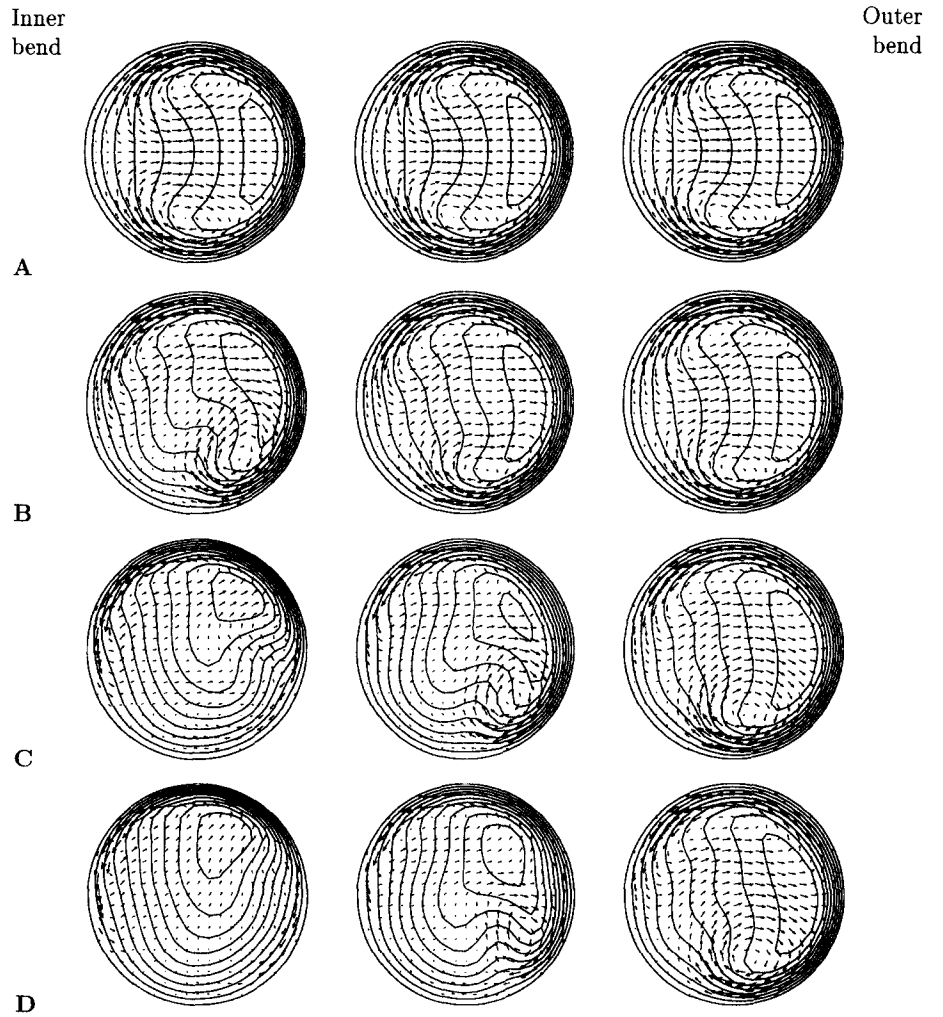

Fig. 4. Computed isotachs and secondary velocity vectors at cross-section $x = 20d$ (left), $x = 50d$ and $x = 100d$ (right) in an isothermally cooled coil for $Re = 500$, $Dn = 134$, $Pr = 5$. (A) $Gr = 0$; (B) $Gr = 10^5$; (C) $Gr = 5 \cdot 10^5$; (D) $Gr = 10^6$. A vector length equal to the radius of the pipe corresponds to the mean axial velocity.

shaped temperature contours have been split into two relatively autonomous warm areas. This splitting is a result of cold medium transported from the pipe wall through the core to the outer wall. Since the thermal diffusivity of water is modest, the cold medium passing the core only is moderately heated by the surrounding warm water and remains colder than the surrounding water when it almost has reached the outer wall. In the centre of the two resulting warm areas the secondary velocity is small and recirculating, and thus diffusion of heat becomes a major mechanism of heat transfer there. Further downstream in Fig. 5A it is seen that the relatively warmer areas remain to exist.

For the case of $Gr = 10^5$ also two relatively warm areas exist for $x = 20d$ and further downstream. The temperature field, however, has become very complex due to the complex secondary flow field here, in which both centrifugal and buoyancy effects manifest themselves. For $Gr = 5 \cdot 10^5$ and $Gr = 10^6$ the velocity field at $x = 20d$ was seen to be largely influenced by buoyancy effects. The secondary flow here was less intense than at lower Grashof numbers, and a splitting up of the temperature contours is not present. The isotherms here exhibit the C-shape. As described, further downstream centrifugal effects become increasingly important. These are observed first near the outer bend where the axial velocity is higher. At $x = 50d$ two warmer areas have formed, which persist at $x = 100d$.

Flow and heat transfer parameters

The rate of heat transfer as a function of axial position in the coil is presented in Fig. 6 by the local Nusselt number. This local Nusselt number is defined as $Nu = (\bar{h} \cdot d/\lambda)$, in which $\bar{h}$ is the heat transfer coefficient averaged over a cross-section. The first $11d$ or 90° of the coil for the cases $Gr = 0$ and $Gr = 10^5$ have been described in refs. [17, 18]. It was explained there that the Nusselt number first decreases, following the forced convective case, then increases, due to the set-up of the secondary flow and then decreases

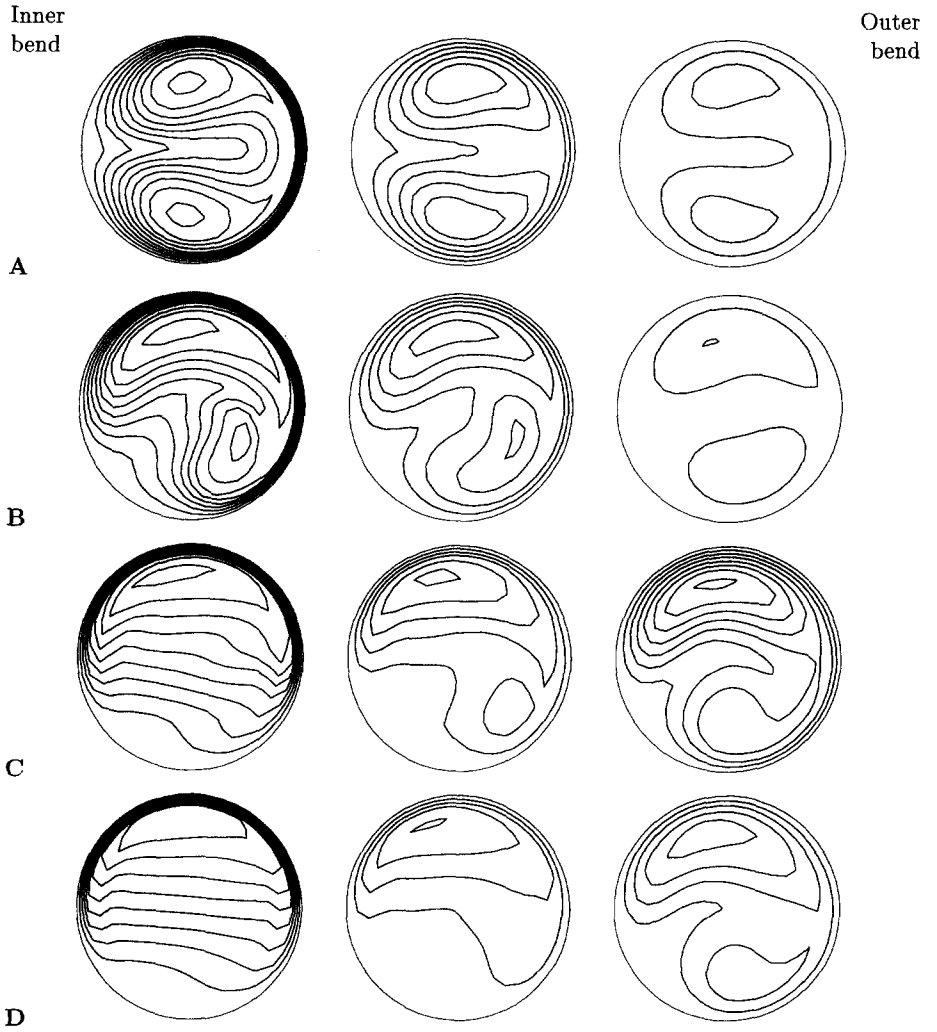

Fig. 5. Computed isotherms at cross-section $x = 20d$ (left), $x = 50d$ and $x = 100d$ (right) in an isothermally cooled coil for $Re = 500$, $Dn = 134$, $Pr = 5$. (A) $Gr = 0$; (B) $Gr = 10^5$; (C) $Gr = 5 \cdot 10^5$; (D) $Gr = 10^6$. The difference between the successive isotherms is 0.1. For $Gr = 5 \cdot 10^5$ and for $Gr = 10^6$ at $x = 100d$ the difference between successive isotherms is 0.02.

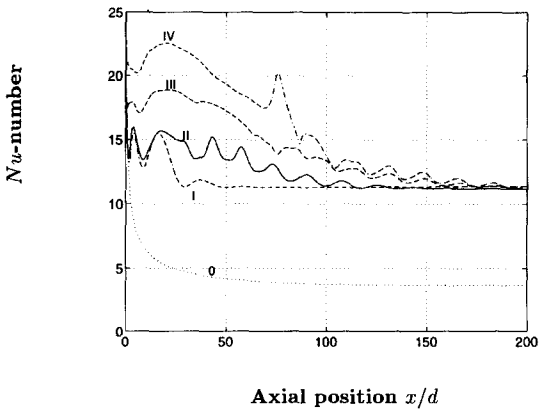

Fig. 6. Nusselt number as a function of the axial position in an isothermally cooled coil for $Re = 500$, $Dn = 134$ and $Pr = 5$: (I) $Gr = 0$; (II) $Gr = 10^5$: (III) $Gr = 5 \cdot 10^5$; (IV) $Gr = 10^6$. As a reference also the Nusselt number for developing forced convection is plotted as the dotted line 0 [19].

again. Mainly due to centrifugal forces, initially a strong secondary flow develops in the core of the pipe, which subsequently passes the lower and upper wall of the pipe. Since the medium associated with this flow is relatively warm, as it originates from the warm core region, heat transfer from the medium to the cold tube increases. Further downstream, the magnitude of the secondary flow near the tube wall decreases, and although relatively warm water is transported along the tube wall, the rate of heat transfer decreases due to the weaker secondary convective effects. From $x = 8d$ the Nusselt number increases again.

For $Gr = 0$ and $Gr = 10^5$ (lines I and II in Fig. 6) it is observed that at $x = 16d$ again a local maximum in the Nusselt number is reached. For $Gr = 0$ this is followed by a local minimum at $x = 29d$, a local maximum at $x = 38d$, and so on, with decreasing difference between maxima and minima. A physical reason for the behaviour of the Nusselt number is

found in the circulating secondary flow along the tube wall, and in a sense it is a reflection of the splitting up phenomenon described previously. Before the flow penetrating through the core of the tube has reached the outer bend, fresh water is conveyed along the pipe wall by the secondary flow. After the penetrating flow has reached the outer bend, water transported along the cold wall has already been there once before, and was cooled then. Referring to Fig. 6, for the case $Gr = 10^5$ a similar wave phenomenon occurs, although the amplitude of the waves is larger than for $Gr = 0$. This can be understood by taking into account that when relatively warm water flows along the cold wall, buoyancy causes the secondary flow to become stronger. As a result, secondary convective effects increase and the waves in the Nusselt number intensify.

For $Gr = 5 \cdot 10^5$ and $Gr = 10^6$ it has been observed that initially the flow is mainly influenced by buoyancy effects and that a relatively weak secondary flow has developed. In the first $75d$ of these cases a wavy behaviour in the Nusselt number is hardly observed, which seems due to the smaller secondary flow. The Nusselt number is substantially higher than for $Gr = 0$ and $Gr = 10^5$, however. Buoyancy effects have seen to cause the fluid in the pipe to be translated towards the upper pipe wall, and here the thermal boundary layer has become very thin, yielding a large heat transfer. It has been described that eventually centrifugal forces take over, and from $x = 75d$ the Nusselt number exhibits a wavy behaviour with an approximately equal wavelength as for $Gr = 0$. Here the secondary flow has become stronger and the splitting up phenomenon occurs. The large peak in the Nusselt number for $Gr = 10^6$ at $x \approx 75d$ may be a consequence of this increase in strength of secondary flow (see also Fig. 8).

Note further that at $x = 200d$, the temperature field is still not fully developed for $Gr = 5 \cdot 10^5$ and $Gr = 10^6$. In the fully developed case, the Nusselt value does no longer change and stabilizes at $Nu = 11.4$ (Fig. 6). This value is also found using the correlation given in ref. [24]: $Nu = 0.836 Dn^{0.5} Pr^{0.1}$ for fully developed forced convection in a curved pipe with uniform wall temperature. The correlation is based on numerical solutions of the equations describing the fully developed flow and is claimed to be valid in the region $0.7 \leqslant Pr \leqslant 5$ and $Dn \geqslant 80$.

In Fig. 7 the axial development of the bulk temperature is given for the cases considered. At the end of the $200d$ coil the water shows to have released more than 95% of its thermal energy contents. Also the bulk temperature development for the Graetz problem is shown (line 0), which shows that at the end of a $200d$ straight tube the energy release is about 75%. The bulk temperatures for $Gr = 0$ and $Gr = 10^5$ deviate only slightly in the first $11d$ of a curved bend. As indicated by Fig. 6, further downstream, from about $x = 20d$, the Nusselt number for $Gr = 10^5$ becomes substantially higher than for $Gr = 0$. This is reflected in the axial evolution of the bulk temperature, where

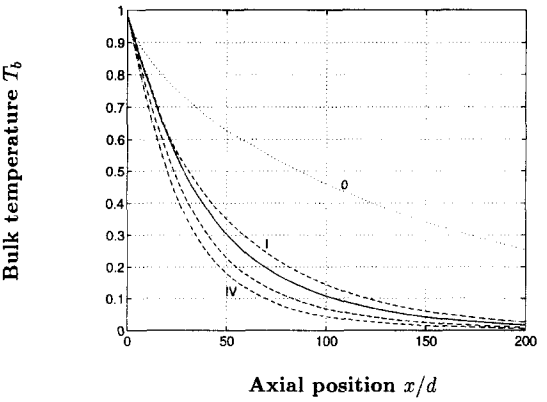

Fig. 7. Dimensionless bulk temperature as a function of axial position in an isothermally cooled coil for $Re = 500$, $Dn = 134$ and $Pr = 5$; (I) $Gr = 0$; (II) $Gr = 10^5$; (III) $Gr = 5 \cdot 10^5$; (IV) $Gr = 10^6$. As a reference also the bulk temperature number for developing forced convection is plotted as the dotted line 0 [19].

line II shows a steeper slope than line I at about $x = 20d$. The lines for the higher Grashof numbers show a steeper slope from the entrance of the bend, and for $Gr = 10^6$ (line IV) the water has lost 75% of its heat at about $40d$.

The development of the magnitude of the secondary flow has been quantified by the K-number defined as:

$$K = \frac{\int_A u_{\text{sec}}^2 \, \mathrm{d}y \, \mathrm{d}z}{\int_A u_{\text{ax}}^2 \, \mathrm{d}y \, \mathrm{d}z}. \tag{16}$$

On the left side of Fig. 8 the initial development (to $x = 20d$) of the K-number is shown. The right side shows the further development. Note that the scaling of the axes between the left and right side is different. The initial growth and decrease of the K-number for $Gr = 0$ and $Gr = 10^5$ has been discussed before in refs. [17, 18] and is related to the onset of centrifugal flow (initial growth) and inertia forces working on the fluid particles (leading to an overshoot and finally a decrease). For $Gr = 10^6$ the relatively large magnitude of the secondary flow near the entrance is due to strong buoyancy effects. Further downstream a similar wavy behaviour as for the Nusselt number is observed. This is again due to the convective circulations of the secondary flow. For $Gr = 10^5$ the waves in the K-number show to correlate well with the waves in the Nusselt number. A high Nusselt number yields stronger buoyancy effects and thus a stronger secondary flow. For higher Grashof numbers the K-number exhibits a continuous decrease from the maximum near the entrance to a minimal value around $x = 30$–$40d$. As will be shown by Fig. 11 the axial evolution of the K-number for $Gr = 10^6$ largely follows the axial evolution of mixed convective flow in a straight tube. It has been indicated previously that the secondary flow is decreased due to the sta-

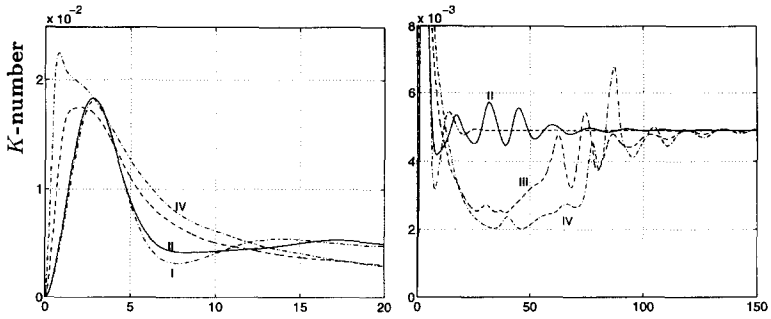

Fig. 8. Relative kinetic energy as a function of axial position in an isothermally cooled coil for $Re = 500$, $Dn = 134$ and $Pr = 5$; (I) $Gr = 0$; (II) $Gr = 10^5$; (III) $Gr = 5 \cdot 10^5$; (IV) $Gr = 10^6$.

bilizing effect of the stratification in the core of the tube. While the medium in the pipe loses its heat, the stratification decreases and centrifugal effects cause the secondary flow to increase. This happens from $x = 40d$, say. From $x \approx 60d$ the wavy behaviour observed in the Nusselt number shows its reflection in the relative kinetic energy of the secondary flow. Finally the K-number stabilizes at $K = 4.9 \cdot 10^{-3}$.

CONCLUDING DISCUSSION

In the present study mixed convection in a helically coiled heat exchanger is studied using a parabolic solution procedure. The code is validated by comparing the results to elliptically computed ones for mixed convection flow in the entrance section of a curved tube. A fair agreement has been found. Next, mixed convection flow in a coil is analyzed over an axial distance of 200 diameters for a fixed Reynolds, Dean and Prandtl number and for a varying Grashof number. In all simulations the coil is set at a lower constant temperature than the inflowing medium. In general it is observed that increasing Grashof numbers lead to enhanced heat transfer and that there is a strong interaction between centrifugal and buoyancy forces leading to complex secondary flow fields.

From the comparison between the elliptic and parabolic results it appeared that for water a third vortex is observed for $Gr = 10^5$ and $Dn = 134$ at position $x = 8d$ (see Fig. 3). At $x = 20d$, however, this vortex has disappeared (see Fig. 4). This seems to be in accordance with the findings of ref. [10], who carried out flow visualization experiments using smoke injection in air. At the outlet of a 180° isothermally heated curved pipe six secondary vortices are observed for $Dn < 600$, of which four vortices remain at $Dn = 425$ and three vortices at $Dn = 304$ and $Dn = 243$ for all Grashof numbers studied. For smaller Dean numbers two vortices were observed.

The splitting up phenomenon of the temperature field, as found in Fig. 5, has also been described by [25], who numerically studied the development of the temperature field in a fully developed velocity field in a curved, isothermally heated pipe. For the case $Pr = 10$ and $Dn = 37.1$, they showed that the 'kidney'-shaped isotherms split up in two 'eyes' of isothermals at $x = 0.298 \cdot Re \cdot d$. Since, in the present case, the secondary flow is substantially stronger ($Dn = 134$), the splitting up phenomenon already occurs before $x = 0.04 \cdot Re \cdot d$. Further, it is interesting to mention that ref. [25] did not observe any splitting up of isotherms for the case of $Pr = 0.7$, in which case the thermal diffusivity is higher and the fluid passing the core is sufficiently heated to avoid the occurrence of the two 'eyes'.

In ref. [11] entry flow in heated curved pipes is studied by dividing the flow domain into two regions: the core region and the boundary layer. The boundary layer flow is solved by expanding the variables in powers of the axial distance and employing a numerical integration method. The analysis is limited by $Gr \ll Re^{5/2}$ (which is not severe) and to small axial distances. The results of Nusselt number and friction factor, however, show clearly an oscillatory behaviour in axial direction. For instance, near the entrance of the pipe the maximum Nusselt number is located at the inner bend, while it shifts towards the outer bend with increasing axial position. This oscillatory behaviour decreases with increasing Prandtl number. The wavy behaviour of the Nusselt number has been observed also in the study of ref. [26], who numerically and experimentally studied the development of the temperature field in a fully developed forced curved pipe flow, subject to a constant wall heat flux, and in the study of ref. [27], who numerically and experimentally studied higher Prandtl number fluids, also for the case of a constant wall temperature. Also in ref. [25] a wavy behaviour is observed, but this was attributed to numerical artifacts.

As mentioned before, a physical reason for the behaviour of the Nusselt number is found in the circulating secondary flow along the tube wall. As can be seen in Fig. 4A, at $x = 20d$ the secondary flow has just made one D-shaped circulation. This explains the local maximum in the Nusselt number at $x = 18d$, which is the axial location where the first circulation

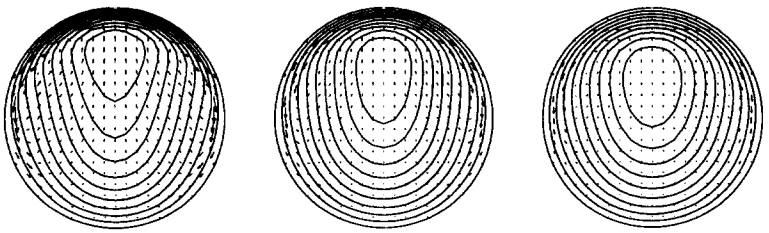

Fig. 9. Computed isotachs and secondary velocity vectors at cross-section $x = 20d$ (left), $x = 50d$ and $x = 100d$ (right) in a isothermally cooled straight tube for $Re = 500$, $Dn = 0$, $Pr = 5$ and $Gr = 10^6$. A vector length equal to the radius of the pipe corresponds to the mean axial velocity.

is finished. The following Nusselt waves are a reflection of the first one. The wavelength, Λ, of this recirculation effect can roughly be approximated by estimating the axial distance that a fluid particle has travelled, while it went through one D-shaped circulation: $\Lambda \approx (\pi/2+1)\ (Re/Dn) \cdot d$ [see equation (1)], and for the present case $\Lambda \approx 10d$. From Fig. 6 it is seen that this indeed is the correct order of magnitude (in fact Λ amounts to about $17.5d$). As was indicated before, the wavy behaviour is correlated to the splitting up phenomenon in the temperature field. Correlating the estimated Λ to the axial distance from the entrance of the coil where splitting up occurs, it is estimated that this may be expected at about $x = 0.02 \cdot Re \cdot d$ for $Dn = 134$ and at about $x = 0.07 \cdot Re \cdot d$ for $Dn = 37.1$, which corresponds reasonably well to the values given in the previous section.

It can be deduced that the splitting up phenomenon is less intense with decreasing Prandtl number and Dean number. In the first case the thermal diffusivity becomes larger and the penetrating cold fluid is heated more. In the second case the cold fluid remains longer in the core region since the secondary flow is less intense and thus the fluid is heated more. In refs. [26, 27] indeed a decrease in the Nusselt wave amplitude with increasing Dn and Pr is reported.

This study has shown that for certain values of the Grashof number, buoyancy effects increase the amplitude of the waves, reflecting the fact that when the heat transfer is higher, also buoyancy effects are higher. When buoyancy effects become more dominant than centrifugal effects, the magnitude of the secondary flow was found to decrease, and the waves in the Nusselt number damp out. This can be attributed to the strong stabilizing effect of the stratification in the pipe.

It has been indicated that the flow in the coiled pipe up to a certain axial distance is largely influenced by buoyancy effects for $Gr = 5 \cdot 10^5$ and $Gr = 10^6$. For $Gr = 10^6$ the considered coiled pipe flow exhibits great similarity to straight pipe flow. By comparing Fig. 4D and Fig. 9 it is indeed observed that centrifugal effects do hardly influence the flow field at $x = 20d$ in the coiled pipe case. The mixed convective flow in the straight tube is characterized by a weak secondary flow, pointing downwards in a thin layer at the upper half of the tube and returning through the full width of the core. The isotachs are egg-shaped and a slow development towards a Hagen–Poiseuille flow is visible at the more downstream positions. In the case of a coiled pipe centrifugal effects were seen to take over gradually.

This also is observed in Figs. 10 and 11 for the development of the Nusselt and K-number. In these figures the dashed lines represent the case of both centrifugal and buoyancy effects, and have been shown before in Figs. 6 and 8. The solid lines represent

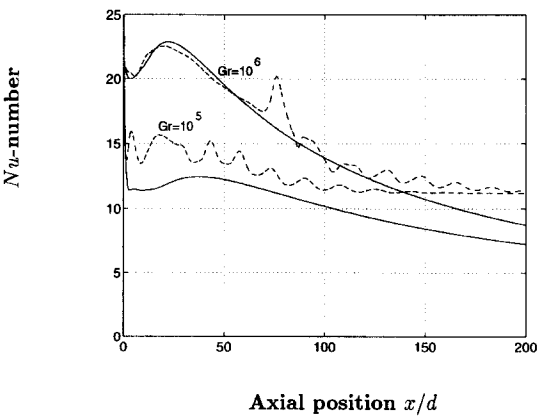

Fig. 10. Nusselt number for $Re = 500$, $Pr = 5$, $Dn = 0$ (—) and $Dn = 134$ (- - -), $Gr = 10^5$ (lower pair of lines) and $Gr = 10^6$ (upper pair of lines).

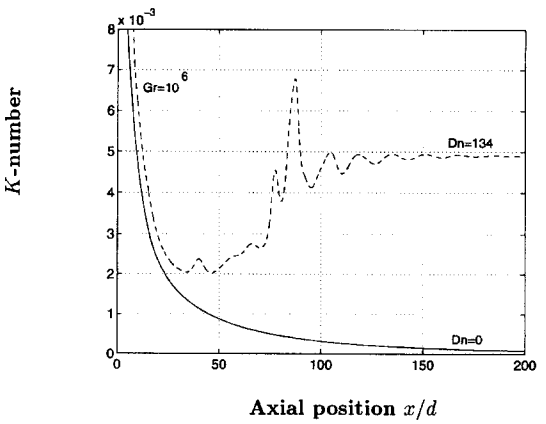

Fig. 11. Relative kinetic energy, for $Re = 500$ $Pr = 5$ and $Gr = 10^6$, $Dn = 0$ (—) and $Dn = 134$ (- - -).

the cases in which only buoyancy effects are active. In Fig. 10 both results for $Gr = 10^5$ and $Gr = 10^6$ are given. It was observed before that for $Gr = 10^5$ the centrifugal effects are dominant. For $Gr = 10^6$ it is seen that buoyancy driven convection is the important heat transfer mechanism. Only for $x > 125d$ the solid and the dashed line start to deviate substantially.

In Fig. 11 it is observed that the solid and dashed lines already deviate from $x \approx 30d$. However, in the curved-tube geometry, the secondary flow resulting from centrifugal effects has only a minor influence on the rate of heat transfer until $x > 125d$. Eventually the solid lines should reach values of $Nu = 3.66$ and $K = 0$, respectively, since buoyancy effects disappear when the medium temperature approaches the wall temperature, and a fully developed Hagen–Poiseuille flow will establish.

It has been shown that it is possible to analyse engineering mixed convective flows using the parabolic solution procedure. However, only a variation in the Grashof number is made here. In order to establish new correlation formula for heat transfer in a coil, an extensive variation of the other parameters characterizing the flow (*Re*, *Dn*, *Pr*) should be made. It has been shown, however, that for the constant temperature case a large part of the flow is in the developing region, and thus general correlations are difficult to derive. This implies also that correlations for the fully developed case are of limited value.

Acknowledgements—This work was sponsored by the Stichting Nationale Computerfaciliteiten (National Computing Facilities, NCF) for the use of supercomputer facilities, with financial support from the Nederlandse Organisatie voor Wetenschappelijk Onderzoek (Netherlands Organisation for Scientific Research, NWO). Besides, the authors are grateful to Dr J. K. B. Krijger who provided a code for solving the parabolized Navier–Stokes equations in a straight tube.

REFERENCES

1. Hollands, K. G. T. and Lightstone, M. F., A review of low-flow, stratified-tank solar water heating systems. *Solar Energy*, 1989, **43**(2), 97–105.
2. Dean, W. R., Note on the motion of fluid in a curved pipe. *Philosophical Magazine*, 1927, **20**, 208–223.
3. Morton, B. R., Laminar convection in uniformly heated horizontal pipes at low Rayleigh numbers. *Quarterly Journal of Mechanics and Applied Mathematics*, 1959, **12**, 410–420.
4. Le Fevre, E. J., Laminar free convection from a vertical surface. *Proceedings of the 9th International Congress of Applied Mechanics*, 1956, **4**, 168–173.
5. Wang, C. Y., On the low-Reynolds-number flow in a helical pipe. *Journal of Fluid Mechanics*, 1981, **108**, 185–194.
6. Chen, W.-H. and Fan, C.-N., Finite element analysis of incompressible viscous flow in a helical pipe. *Computational Mechanics*, 1986, **1**, 281–292.
7. Lee, J.-B., Simon, H. A. and Chow, J. C. F., Buoyancy in developed laminar curved tube flows. *International Journal of Heat and Mass Transfer*, 1985, **28**(3), 631–640.
8. Prusa, J. and Yao, L.-S., Numerical solution for fully developed flow in heated curved tubes. *Journal of Fluid Mechanics*, 1982, **123**, 503–522.
9. Yao, L.-S. and Berger, S. A., Flow in heated curved pipes. *Journal of Fluid Mechanics*, 1978, **88**(2), 339–354.
10. Cheng, K. C. and Yuen, F. P., Flow visualization experiments on secondary flow patterns in an isothermally heated curved pipe. *Journal of Heat Transfer*, 1987, **109**, 55–61.
11. Padmanabhan, N., Entry flow in heated curved pipes. *International Journal of Heat and Mass Transfer*, 1987, **30**(7), 1453–1463.
12. Fletcher, C. A. J., *Computational Techniques for Fluid Dynamics*. Springer, Berlin, 1991.
13. Patankar, S. V., Pratap, V. S. and Spalding, D. B., Prediction of laminar flow and heat transfer in helically coiled pipes. *Journal of Fluid Mechanics*, 1974, **62**(3), 539–551.
14. Krijger, J. K. B., Computational hemodynamics of the basilar artery. Ph.D. thesis, Rijksuniversiteit Groningen, 1991.
15. Hirsch, Ch., *Numerical Computation of Internal and External Flows*. Wiley, New York, 1988.
16. Briley, W. R., Numerical method for predicting three-dimensional steady viscous flow in ducts. *Journal of Computer Physics*, 1974, **14**, 8–28.
17. Sillekens, J. J. M., Rindt, C. C. M. and Van Steenhoven, A. A., Mixed convection in a 90° horizontal bend. In *Proceedings of 10th International Heat Transfer Conference*, ed. G. F. Hewitt, Vol. 5, 1994, pp. 567–572.
18. Sillekens, J. J. M., Rindt, C. C. M. and Van Steenhoven, A. A., Mixed convective heat transfer in a horizontal bend. In *Advanced Concepts and Techniques in Thermal Modelling, Proceedings of Eurotherm* 36, 1994.
19. Shah, R. K. and London, A. L., *Laminar Flow Forced Convection in Ducts*. Academic Press, New York, 1978.
20. Hornbeck, R. W., An all-numerical method for heat transfer in the inlet of a tube. *American Society of Mechanical Engineering*, 1965, **65-WA/HT-36**.
21. Turner, J. S., *Buoyancy Effects in Fluids*. Cambridge University Press, Cambridge, 1973.
22. Opstelten, I. J., Experimental study on transition characteristics of natural-convection flow. Ph.D. thesis, Delft University of Technology, The Netherlands, 1994.
23. Goering, D. J. and Humphrey, J. A. C., On the spatial stability of tube flows subject to body forces. *Physics Fluids. A.*, 1993, **5**(12), 3107–3121.
24. Kalb, C. E. and Seader, J. D., Fully developed viscous-flow heat transfer in curved circular tubes with uniform wall temperature. *AIChE Journal*, 1974, **20**(2), 340–346.
25. Akiyama, M. and Cheng, K. C., Laminar forced convection in the thermal entrance region of curved pipes with uniform wall temperature. *Canadian Journal of Engineering*, 1974, **52**, 234–240.
26. Dravid, A. N., Smith, K. A., Merril, E. W. and Brian, P. L. T., Effect of secondary fluid motion on laminar flow heat transfer in helically coiled tubes. *AIChE Journal*, 1971, **17**(5), 1114–1122.
27. Janssen, L. A. M. and Hoogendoorn, C. J., Laminar convective heat transfer in helical coiled tubes. *International Journal of Heat and Mass Transfer*, 1978, **21**, 1197–1206.